JOURNAL OF SPACECRAFT AND ROCKETS
Vol. 33, No. 1, January–February 1996

Grid-Resolved Analysis of Base Flowfield for Four-Engine Clustered Nozzle Configuration

Ten-See Wang*
NASA Marshall Space Flight Center, Huntsville, Alabama 35812

The objective of this study is to develop and to anchor a computational methodology for the base flowfield of a four-engine clustered nozzle configuration. This computational methodology is based on a three-dimensional, viscous-flow, pressure-based computational-fluid-dynamics formulation. For efficient computation, a Prandtl–Meyer solution treatment is applied to the algebraic grid lines near nozzle lip for resolution of the initial plume expansion angle. As the solution evolves, the computational grid is solution-adapted according to pertinent flowfield parameters. The model employs a formally second-order-accurate adaptive upwind scheme in which second- and fourth-order central-differencing schemes with minimal dissipation are used. Qualitative clustered-nozzle base-flow features such as the reverse jet, plume-to-plume recompression shock, base recompression, and vent-area choking were numerically captured. The computed quantitative base-flow properties such as the radial base pressure distributions, model centerline static pressure, Mach-number and impact-pressure variations, and characteristic curve of base pressure vs ambient pressure agreed reasonably well with those of the measurement. The pertinent clustered-nozzle base-flow physics are highlighted and described in detail by comparing the numerical computations with appropriate test results.

Nomenclature

A_c	= area bounded by nozzles and theoretical vent area in the exit plane
A_v	= theoretical vent area located at the narrowest section between nozzles
C_1, C_2, C_μ	= turbulence modeling constants, 1.44, 1.92, and 0.09
G	= geometrical matrices
h	= enthalpy
J	= Jacobian of coordinate transformation
k	= turbulent kinetic energy
M	= Mach number
P	= pressure
P_r	= turbulent kinetic energy production
q	= $1, u, v, w, h, k$, or ε
S_q	= source term for equation q
t	= time
U	= volume-weighted contravariant velocity
u_τ	= friction velocity, $(\tau_w/\rho)^{1/2}$
u^+	= nondimensional u velocity, u/u_τ
u, v, w	= mean velocities in x, y, and z directions
x, y, z	= physical coordinates
y^+	= nondimensional distance from the wall, $yu_\tau\rho/\mu$
α	= conical nozzle half angle, 17.8 deg
β	= Prandtl–Meyer expansion angle
ε	= turbulent kinetic energy dissipation rate
θ	= initial plume expansion angle
μ	= effective viscosity
ξ	= computational coordinates
ρ	= density
σ_q	= turbulence modeling constants
τ_w	= wall shear stress
Φ	= energy dissipation function

Subscripts

a	= ambient or test cell
b	= base
bc	= model centerline property on base
e	= nozzle exit
I	= impact probe property
w	= wall
0	= nozzle total property

Received Jan. 18, 1995; revision received Aug. 30, 1995; accepted for publication Sept. 3, 1995.

*Researcher, Computational Fluid Dynamics Branch. Member AIAA.

Introduction

EXCESSIVE base heating has been a problem for many launch vehicles[1] using clustered engines. For certain designs such as the direct dump of turbine exhaust inside and at the lip of the nozzle,[2] the potential burning of the turbine exhaust in the base region can be of great concern.[3] Therefore, accurate prediction of the base environment at altitude is very important during the vehicle design phase. Improper account of the base heating phenomena can lead to undesirable consequences. In the recent past, the base environments of launch vehicles have been predicted with large uncertainties using empirical methods. Those uncertainties could lead to out-of-database extrapolations or to overly conservative designs of the thermal protection system, and hence to reduced payloads. Experimental methods can be designed, but the analyst must be concerned with simulation technique and scaling considerations, both of which have a high degree of uncertainty.[4,5] The computational fluid dynamics (CFD) method, which can be accurate over a range of conditions when anchored with well-designed experiments, may provide an useful design tool. In fact, Brewer and Craven[6] stated that ultimately the finite difference computational techniques have the best chance of solving the clustered-engine base-flow problem.

However, to benchmark a computational methodology for clustered-engine base flows, accurate experimental data that reveal the correct physics must be used. The base-flow physics of the axisymmetric single engine has often been confused with the three-dimensional clustered-engine base-flow physics. The differences are significant and require some clarification. Research into the single-engine base-flow phenomena can be categorized into studies with a central jet (power on), e.g., the missile-type afterbody flows, and those without a central jet (power off) e.g., the planar backward-facing step flows. A large number of analytical, experimental, and computational studies have been reported for the single-engine-type flows, and surveys can be found in Refs. 4, 7, and 8. At low altitudes, the single-engine base-flow physics is driven by either the recirculating flow caused by the interaction of external flow and base (power off), or the aspirating flow entrained by the central jet

and the subsequent reduction of power-off pressure, or the recirculating flow caused by the plume–base–external-flow interactions. As the plume expands in size and as the altitude increases, the plume begins to deflect the external flow and to generate a rise in base pressure that communicates upstream through the surface boundary layer. Consequently, the viscous layer separates some distance forward of the base and generates a plume-induced flow separation.

Multiple-engine clustered-nozzle base-flow physics retains the single-engine base-flow components of aspirating flow, recirculating flow, and plume-induced flow separation, albeit all three-dimensionally. Additionally, the participating plumes impinge upon each other as they expand, and deflect a portion of the plume boundary into the base, forming a base-impinging reverse jet. Three or more nozzles can reverse enough exhaust gas at high altitudes that the reverse jet goes supersonic and a wall jet forms. The wall jet chokes at certain altitudes. This reverse jet and the accompanying wall-jet choking phenomena are unique to the multiple-engine clustered-nozzle base-flow physics. When carrying high-temperature combustible exhaust gases, this reverse jet can burn the base like a flame torch. As an example of misrepresentation of the physics, several Korst–Chapman[9] viscous-theory-based component flow models have been proposed[4] to predict the reverse jet. However, as noted by Brewer and Craven[6] and later computationally confirmed by Wang,[10] the reverse jet forms even in three-dimensional inviscid flow. Thus, using the two-dimensional shear-layer analysis for the reverse-jet calculation is potentially misleading, especially when extrapolating the database.

Because of the difficulties in simulation and scaling, cost, and (to some degree) misconception of the flow physics, few benchmark-quality clustered-nozzle base-flow experiments[6,11–13] have been performed. However, some flight data[14,15] do exist. The complex three-dimensionality of the flow physics has not only made analytical studies infeasible, but also made computational studies, only a few of which have been conducted to date, a formidable task. Cain et al.[16] made a comparison of the axial pitot pressure for a four-nozzle cluster based on inviscid and experimental results. However, the action area is downstream from the plume interaction for the plume signature rather than for the near-base flowfield. Dougherty and Liu[17] computed one base pressure coefficient for the three-engine Space Shuttle Orbiter aft heat shield and compared it with the ascent flight data. The computed value lies in the band of flight data at the same Mach number; however, the altitude simulated was 250,000 ft instead of 35,000 ft. Holcomb[18] conducted two qualitative base-flowfield computations for a four-engine Minuteman first stage and a two-engine Titan first stage. Sindir and Lynch[19] computed base pressures for a six-engine National Launch System 1.5-stage configuration at two altitudes. All four groups of investigators[16–19] used single-engine plume–base-flow physics to benchmark their codes. The first numerical benchmarking effort for a multiple-engine clustered-nozzle base-flow investigation was performed by Wang.[10] In that study, the turbulent base flowfield of a cold-flow experimental investigation[6] for a four-engine clustered nozzle was numerically benchmarked. This was a necessary step before the benchmarking of combustion flow tests could be considered. The experiment was conducted in a quiescent environment to avoid external-flow influence, and flow physics unique to the multiple-engine nozzle cluster can be investigated. Quantitative results such as the radial base pressure distribution and the Mach-number and static-pressure variations along the model centerline were computed for a selected ambient-to-total pressure ratio (P_a/P_0) of 39×10^{-4}. The inviscid nature of the reverse jet was captured through a Prandtl–Meyer-solution treatment of the initial plume expansion. Those predictions agreed reasonably well with the measurement,[6] though rather coarse and unadapted grids were used. However, those results can be improved, and the present effort is an extension of that work.

Obviously, as noted in Ref. 10, the grid resolution played a dominant role in determining the accuracy of any base-flow solution. Higher grid density often resulted in better predictions. However, in the study of complicated three-dimensional clustered-nozzle base-flow physics, balancing the cost and the accuracy of the solution[20] and even the availability of computer resources have become critical issues. Hence, one must develop methods that are capable of effectively increasing the spatial resolution without excessive refinement of the overall grid. This goal is achieved by expanding the appropriate initial Prandtl–Meyer expansion grid resolution[10] at each altitude and by adapting the computational grid to the flow solution according to relevant base-flow physics. A rational pressure-based CFD formulation is used to solve the plume–base flowfield. Pertinent clustered-nozzle base-flow features such as the radial base pressure distributions, model centerline Mach-number and pressure variations, and base pressure characteristic curve are computed and compared with the experiment on a expanded database. Features unique to the multiple-engine clustered-nozzle base flow, such as the vent-area choking and characteristic-curve reversal, are obtained with the proposed computational methodology.

Governing Equations and Solution Algorithm

The basic equations employed to describe the base flowfield for a four-engine clustered nozzle are the three-dimensional, general-coordinate transport equations. A generalized form of these equations is given by

$$\frac{1}{J}\frac{\partial \rho q}{\partial t} = \frac{\partial[-\rho U q + (\mu/\sigma_q)G(\partial q/\partial \xi)]}{\partial \xi} + \left(\frac{1}{J}\right)S_q \qquad (1)$$

A standard two-equation k–ε turbulence-model[21] closure with a modified wall function is used to describe the turbulent flow. The k–ε model achieves closure by relating the Reynolds stresses to the mean strain rate through the Boussinesq approximation. The effective eddy viscosity, $\mu = \rho C_\mu k^2/\varepsilon$, is computed by solving the k and ε transport equations. Though several other more sophisticated turbulence models have been considered, no single turbulence model has emerged as general enough for all the complex flow physics. In fact, a rational turbulence modeling strategy would be to select the model best suited to describe the main flow physics of current interest—the reverse jet. Accordingly, several versions of the k–ε model, including high- and low-Reynolds-number formulations, have been examined for performance in a U duct.[22]

All the models that were tuned for backward-facing step flows have predicted reasonable recirculating-flow properties before the reattachment point, as they were originally designed. However, they also underpredicted the development of turbulence after the reattachment.[22] On the other hand, the standard k–ε model with wall-function treatment predicted reasonable postreattachment flow development.[22] Note that the flow development after the reattachment point in recirculating flows is closely associated with that of the reverse jet beneath the multiple-plume impingement point. Furthermore, in the context of the current four-engine nozzle-cluster base flow, the physics of the prereattachment backward-facing step flow plays a very minor role.[6]

Low-Reynolds-number turbulence models that integrate to the wall were not considered at this time. The wall boundary layer has a weak effect in the multiple-engine clustered-nozzle base-flow physics. Thus, the detail gained from these models was not deemed to be worth the extra cost here. Besides, their performance benefits over the high-Reynolds-number approach were considered marginal, even for recirculating flows prior to the flow reattachment.[22] These arguments led to the selection of the high-Reynolds-number standard k–ε model for this task. The solution methodology developed in this study does not preclude use of other turbulence model formulations, as long as they describe the physics with sufficient accuracy.

Turbulence modeling constants σ_q and source terms are given in Table 1. These turbulence modeling constants are widely used for nozzle and combustion driven flows.[8,23–26]

A modified wall-function approach[23] is employed to provide near-wall resolution that is less sensitive to the near-wall grid spacing. The term modified indicates that this approach has the grid-saving nature of the conventional law-of-the-wall approach,[21] while allowing the off-wall grid points to reside in the sublayer region. Consequently, the model has combined the advantages of both the

Table 1 σ_q and S_q of the transport equations

q	σ_q	S_q
1	1.00	0
u	1.00	$-P_x + \nabla[\mu(u_j)_x] - \frac{2}{3}(\mu\nabla u_j)_x$
v	1.00	$-P_y + \nabla[\mu(u_j)_y] - \frac{2}{3}(\mu\nabla u_j)_y$
w	1.00	$-P_z + \nabla[\mu(u_j)_z] - \frac{2}{3}(\mu\nabla u_j)_z$
h	0.95	$DP/Dt + \Phi$
k	1.00	$\rho(P_r - \varepsilon)$
ε	1.30	$\rho(\varepsilon/k)(C_1P_r - C_2\varepsilon)$

integrated-to-the-wall approach and the conventional law-of-the-wall approach by incorporating a complete velocity profile[27] given by

$$u^+ = \ell_n\left[\frac{(y^+ + 11)^{4.02}}{(y^{+2} - 7.37y^+ + 83.3)^{0.79}}\right] + 5.63\tan^{-1}(0.12y^+ - 0.441) - 3.81 \quad (2)$$

This complete velocity profile provides a smooth transition between logarithmic law-of-the-wall and linear viscous sublayer velocity distributions. Although it was established for an incompressible, attached flow over a flat surface, the profile can be applied for compressible flow, since the compressibility is addressed by solving the equation of continuity and the rest of the transport equations. It can also be applied to flows over any three-dimensional surface, since any curved surface reduces to an approximately flat surface when magnified. Moreover, the complete velocity profile only applies to the off-wall grid point and is applied in an implicit fashion. That is, the velocity derived from the complete velocity profile is decomposed into appropriate tangential components. These components are then integrated into the source term of momentum equations so that momentum is conserved.

Accurate flow reversal is driven by the local momentum balance, regardless of whether the velocity at the off-wall point is calculated from a universal profile or by integration to the wall. Thus, the present approach achieves computational efficiency by eliminating the low-Reynolds-number terms needed for integration to the wall. An equally computationally efficient energy wall function[23] is also implemented, but not invoked, since a cold-flow experiment[6] was modeled. Its accuracy has been documented in other studies.[23,26,28] Conceptually, it could be used to predict the convective base heat flux in hot-fire experiment or actual rocket firings. The methodology developed in this study, though, can be used to provide valuable base flow properties, which are otherwise unattainable, as inputs to the engineering methods for much-improved base heating predictions.

The equation of state for an ideal gas is employed for the closure of the above system of equations. The characteristic of the governing equations changes from mixed parabolic–hyperbolic for subsonic flows, to mainly hyperbolic for supersonic flows.[25] To solve the system of nonlinear partial differential equations, finite difference approximations were used to establish a system of linearized algebraic equations. An adaptive upwind scheme was employed to approximate the convective terms of the momentum, energy, and continuity equations. The scheme is based on second- and fourth-order central differencing with minimal dissipation. The dissipation terms are constructed so that a fourth-order central and fourth-order damping scheme is activated in smooth regions, and a second-order central and second-order damping scheme is used near shock waves. A total variation diminishing (TVD) scheme can be used; however, it may yield slow-moving shocks or carbuncle shocks,[17,29,30] or force shocks in a weak compression such as a smeared[6] or dissipative[31] base recompression. The central-difference-based upwind scheme was used instead.

Viscous fluxes and source terms are discretized using a second-order central-difference approximation. A pressure-based predictor plus multiple-corrector solution method is employed so that flow over a wide speed range—that is, from the low subsonic base flow to the supersonic plume and the subsequent supersonic reverse jet and the sonic wall jets—can be analyzed. The basic idea of this pressure-based method is to perform corrections for the pressure and velocity fields by solving a pressure correction equation so that velocity–pressure coupling is enforced, constrained by continuity after each iteration. Details of the present numerical methodology are given by Ref. 25.

Baseline Grid Generation

A typical layout of an unadapted computational grid used to simulate the experimental work[6] is shown in Fig. 1. Because of the symmetry of the flowfield, only one-eighth of this layout is generated and used for the actual calculation. The two sides of the pie-shaped grid in Fig. 1 are the symmetry planes. For clarity, the symmetry plane that lies between the nozzles is termed the plume impingement symmetry plane, since the plume impingement line and the attached portion of the plume-to-plume recompression shock will be on or attached to this surface. The other one is termed the nozzle symmetry plane, since it passes through the centerline of the nozzle. The vertical centerline at which the two symmetry planes intersect is termed the model centerline.

Two computational grid zones were created. The first zone started at the base and included the nozzle and the plume-to-plume interaction region. The second zone (the outer shell) is composed of the ambient air and a portion of the expanded plume. On the base-plane grid arrangement, it can be seen that the grid lines are clustered in the base-flow action area, i.e., the reverse-jet impingement and vent areas, and hence the plume impingement and the reverse-jet regions above the base plate, to improve the resolution of the computed base-flow physics. Information on the base-flow action area is gained by utilizing the unadapted-grid flow results from Ref. 10. It can also be seen that the grid lines emanate radially from the nozzle centerline towards the symmetry planes and the surroundings. This C-grid layout ensures the circumferential grid-line symmetry about the nozzle centerline, while the latticelike H-grid reported in Ref. 16 tends to lose that symmetry and thus run the risk of skewing the plume development. The baseline unadapted grids were generated using a GENIE++ grid generator.[32]

The four nozzles, which are conical with a cylindrical external shell, are equally spaced on a circular base (heat shield),[6] as shown in Fig. 2. The area ratio of the nozzles is 3.11:1, and the nozzle exit diameters are 2.67 in. The base is located 2.0 in. from the nozzle exit plane, giving a theoretical minimum vent area between nozzles of approximately 2.0 × 2.0 in. The radial location of the theoretical minimum vent area, consisting of four planes perpendicular to

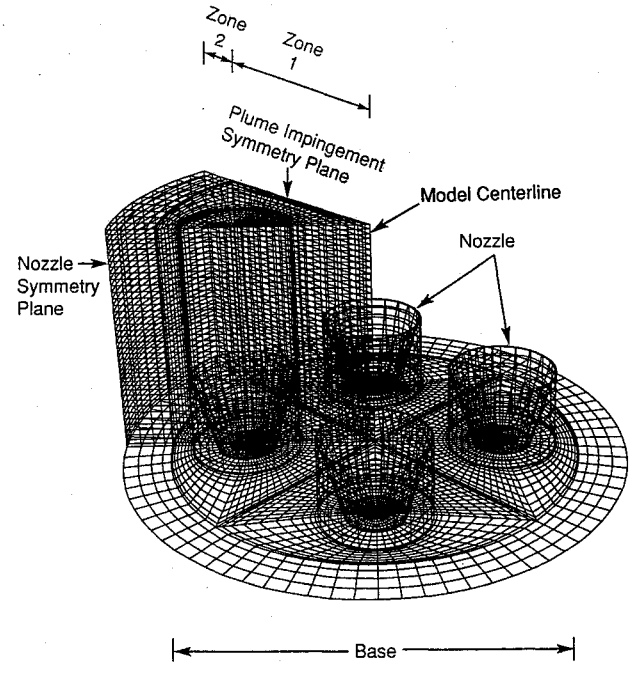

Fig. 1 Layout of a typical computational grid.

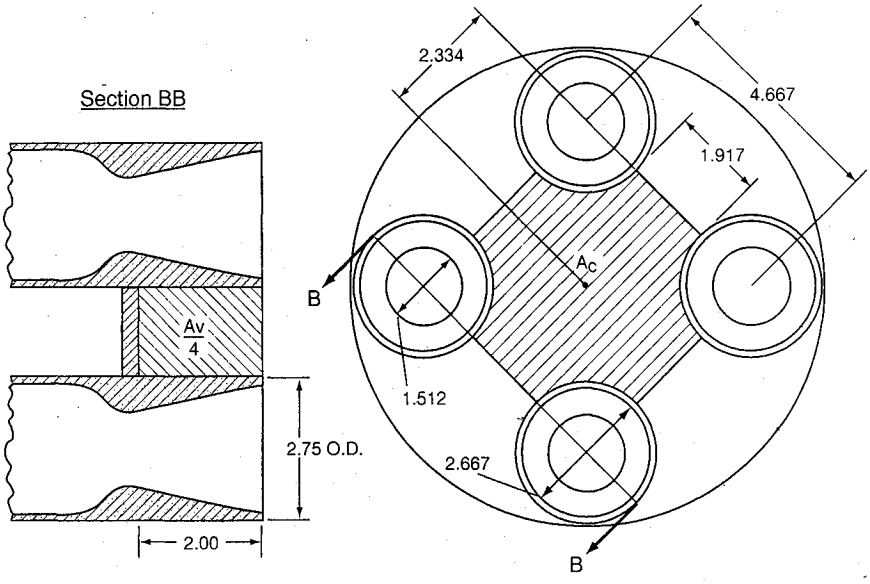

Fig. 2 Model configuration (dimensions in inches).

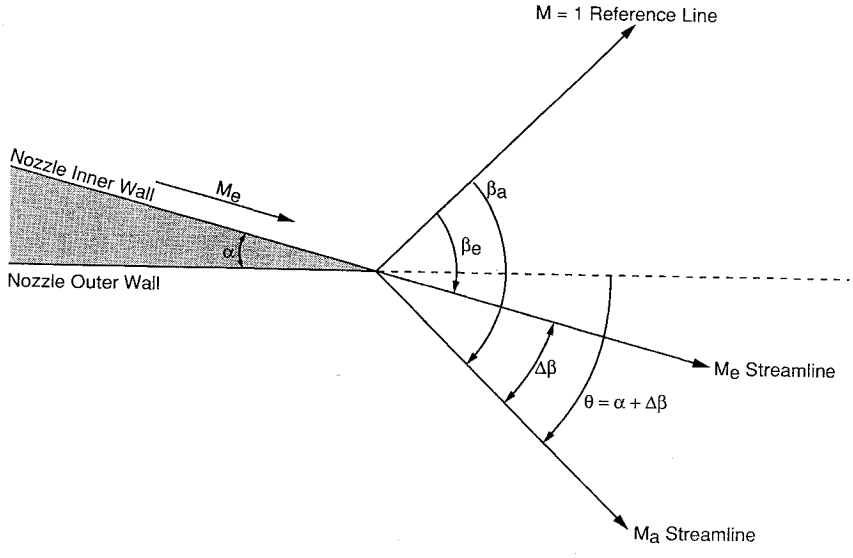

Fig. 3 Prandtl–Meyer expansion around the nozzle lip.

the base and between nozzles, is approximately 2.334 in. from the centerline, which gives a vent area ratio (A_v/A_c) of approximately 0.96. This model is a larger-scale model than the one used in Ref. 11.

Boundary Conditions

To start the calculation, an axisymmetric nozzle flow solution at the prescribed total pressure was carried out separately. A typical centerline exit Mach number for a total pressure of 60 psia was computed as 2.62. The converged flow solution was then mapped to a three-dimensional nozzle flowfield, and the nozzle exit flow properties were specified as a fixed inlet boundary. The computational domain of the axisymmetric nozzle flow calculation started from the subsonic chamber, as shown in section *BB* of Fig. 2, to ensure correct nozzle exit flow properties. These properties include internal boundary-layer growth, nozzle shock strength and location, and turbulence that is generated from the velocity gradient inside the nozzle. This procedure is critical in that it partially determines the outcome of the subsequent base-flow calculation. An example of the importance of using an appropriate solution involves the benchmark efforts for a power-on single-engine base flowfield. Chen et al.[33] obtained good missile base-pressure data comparisons by extending the computational domain back to the chamber of the propulsive nozzle, among other factors. Childs and Caruso[34] conducted identical base-flow calculations, but obtained very different results. These results may be explained by comparison of their solution with the experimental data. The computed flow vectors[34] near the nozzle exit showed neither a boundary layer nor shock, whereas the flow vectors of the experiment exhibited both. Hence, it seems the compromise of the propulsive nozzle properties has adversely affected their conclusions. The importance in achieving the detail of the nozzle exit flow properties is obvious, since the propulsive nozzle flow is the sole source for the plume interaction and the subsequent base-flow phenomena.

The nozzle lip, nozzle outer wall, and base were specified as no-slip wall boundaries, and a tangency condition was imposed on the symmetry planes. The exit planes of zone 1 and zone 2, the outer surface (shell) of zone 2, and the inlet plane of zone 2 (flush with the base shield plane) were specified as exit boundaries. In addition, a fixed (ambient) pressure was imposed on the inlet plane of zone 2, to obtain a unique solution for the corresponding altitude. The flow properties at the wall, symmetry plane, and exit boundary were extrapolated from those of the interior using a second-order formulation.

Prandtl–Meyer Solution Treatment for Resolution of the Initial Plume Angle

It has been shown[10] that the grid resolution for the initial plume angle is essential to the accurate prediction of base-flow properties.

In that study, the predicted base-flow properties showed vast improvement even though a fixed initial plume angle (based on the Prandtl–Meyer solution for $P_a/P_0 = 39 \times 10^{-4}$) was used. The natural extension of that work would be to construct an algebraic grid for the plume for each pressure ratio according to the plume-angle prediction from isentropic Prandtl–Meyer plume expansion theory. As shown in Fig. 3, the initial plume expansion angle can be expressed as $\theta = \alpha + \Delta\beta$, where β is the Prandtl–Meyer expansion angle[35] through which a supersonic stream is turned to expand from $M = 1$ to $M > 1$. Here β_e is based on the nozzle exit Mach number, which may be calculated from a simple one-dimensional model.[36] β_a is based on the ambient-to-total pressure ratio, which is equivalent to having M_a on the plume boundary. The computational efficiency gained from this Prandtl–Meyer expansion treatment verifies the inviscid nature[6] of the four-engine clustered-nozzle base flow.

Solution-Adaptive Grid Generation

The multizone self-adaptive grid evolution (SAGE) code[37] is used to refine the initial plume-angle-resolved algebraic computational grid. The method is based on grid-point redistribution through local error minimization. The procedure is analogous to applying tension and torsion spring forces proportional to the local flow gradient at every point and finding the equilibrium position of the resulting system of grid points. Since the Mach number contour is closely associated with the plume boundary layer, and the pressure gradient follows the recompression shock, these two flowfield variables were used as pertinent grid-adaptation parameters. The adaptive function may be an arbitrary combination of both.

Figure 4 shows slices of four typical computational grids. Each slice is a portion of the nozzle symmetry plane and is bounded by the nozzle centerline and the model centerline. Grid *A* is an algebraic grid treated with the Prandtl–Meyer solution for the initial plume-angle resolution. Grid *B* is the result of adapting grid *A* solely to a pressure solution. The clustered grid lines clearly exhibit the detached portion of the plume-to-plume recompression shock. It should be noted that the adaptation was applied several grid lines above the nozzle lip so as to maintain the initial Prandtl–Meyer expansion-angle resolution. The transition from the unadapted grid lines to the adapted grid lines is smooth. Grid *C* is the outcome of adapting grid *A* entirely to a Mach-number solution. The packed grid lines match the plume boundary and appear to follow the Prandtl–Meyer expansion angle from the nozzle lip. Grid *D* comes from the adaptation of grid *A* where 50% Mach-number gradient and 50% pressure gradient were used as the adaptive function. The grid-line clustering follows both the plume boundary layer and the recompression shock.

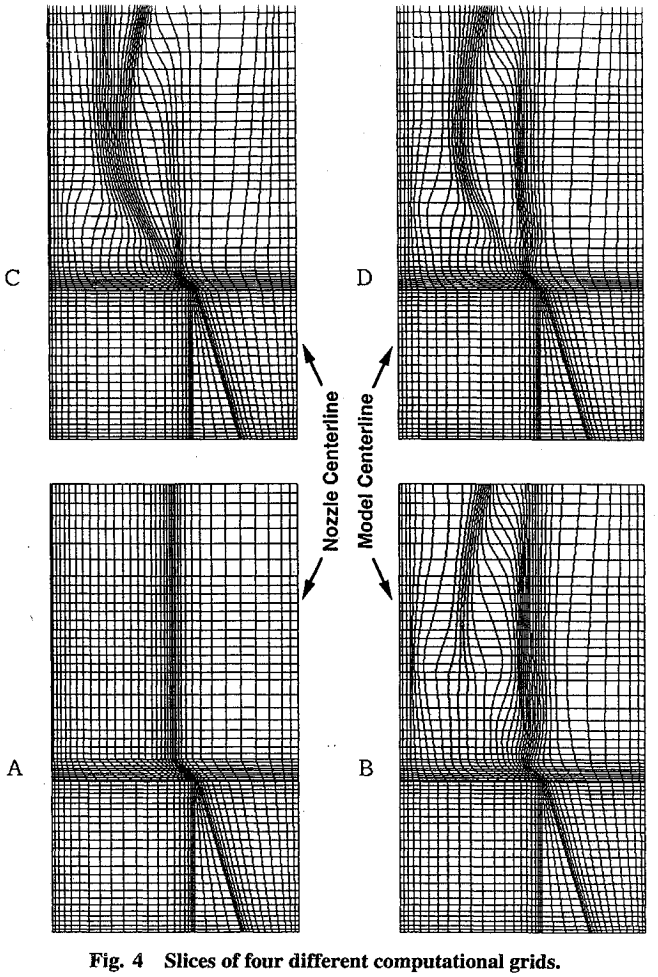

Fig. 4 Slices of four different computational grids.

Results and Discussion

The computations were performed on a NASA/MSFC Cray Y-MP. The computational time for a typical calculation was estimated as 1.0×10^{-4} CPU seconds per grid per step. Approximate convergence was reached when the residual of the vectors was below 1.0×10^{-4} and those of the scalars were under 1.0×10^{-6}. The residuals for the momentum and energy are the root mean squares, and those for other scalars are maximum residuals. Based on present grid-parametric studies and those found in Ref. 10, approximate grid-independent solutions were obtained for grid densities of 113,202 points and of 119,016 points when the Prandtl–Meyer expansion resolution was satisfied. Approximately 3000–4000 iterations were required for a 119,016-grid-point solution to reach approximate convergence, and an additional 2000 iterations were needed for a higher-grid-density (e.g., 168,399 grid points) solution to converge when the initial flowfields were started afresh. The storage requirement of the CFD model is 40 words per grid point. Although the functional memory has increased from that of a Cray-XMP,[10] the cost[20] issue looms if Prandtl–Meyer expansion resolution, turbulence law-of-the-wall approach, and solution-adaptive grid procedure are not considered.

Static-Pressure, Mach-Number, and Impact-Pressure Variations Along the Model Centerline

Static-pressure, Mach-number, and impact-pressure comparisons along the model centerline were used to assess the accuracy of the model prediction of the reverse jet. The creation of the reverse jet originates from the lateral flow emanating from behind the detached shock portion of the plume impingement,[6,10] whereas the strength of the reverse jet comes from the Prandtl–Meyer expansion, the deflection of the free shear layer, and the flow physics inside the plume-to-plume impingement region. The viscous flow emanating from the attached shock portion of the plume impingement region does not significantly affect the base environment and is pumped from the base region by the reverse jet and wall jet.

Figure 5 shows a comparison of variations along the model centerline for $P_a/P_0 = 39 \times 10^{-4}$. The effects of the Prandtl–Meyer solution treatment for the initial plume-angle resolution and solution-adaptive gridding are obvious. The solution with the highest grid density (245,493 grid points)—in which the initial plume expansion was not adequately resolved, even though it employed twice the number of points in the initial plume boundary layer than in the 119,016-point setup and had the grid refined according to the pressure gradient—produced the worst comparison. In contrast, the solutions adapted to a 45.4-deg initial plume angle, including one solution that ran without any further grid adaptation, produced significantly better agreement with less than half the grid points. Among the three solutions, the one using pressure-solution gradient adaptation produced the best centerline-property comparisons with experiment. The one using Mach-number-solution gradient adaptation did not compare as well. This performance difference can be explained by the existence of the plume-to-plume recompression shock, which controls the properties of the reverse jet. The base center pressure, however, was close for all three cases.

This example clearly demonstrates the validity and efficiency of the proposed computational methodology. That is, the accuracy of the reverse-jet prediction depends predominately on the Prandtl–Meyer expansion resolution. This expansion cannot be obtained efficiently with unadapted grid clustering or a solution-adaptive grid

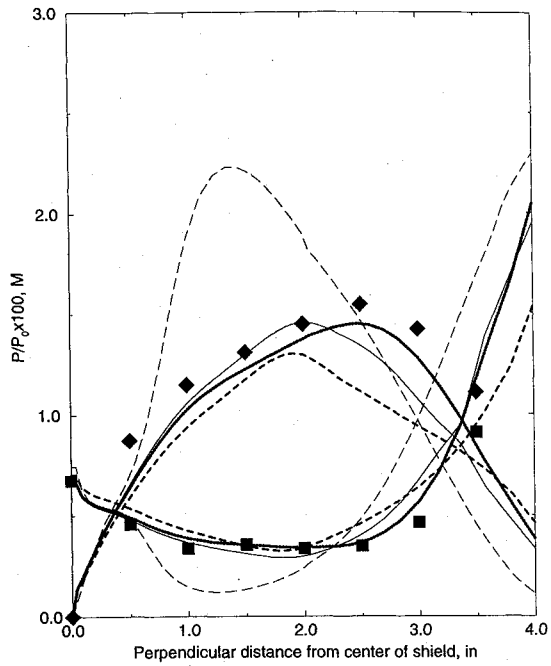

Fig. 5 Comparison of Mach-number and static-pressure variations along model centerline for $P_a/P_0 = 39 \times 10^{-4}$: ■; P/P_0 test data[6]; ♦, Mach number test data[6]; ——, $\theta = 45.4$ deg, 119,016 pts, no adaptation; ——, $\theta = 45.4$ deg, 119,016 pts, P adaptation; – – –, $\theta = 45.4$ deg, 119,016 pts, M adaptation; and – – –, $\theta = 0.0$ deg, 245,493 pts, P adaptation.

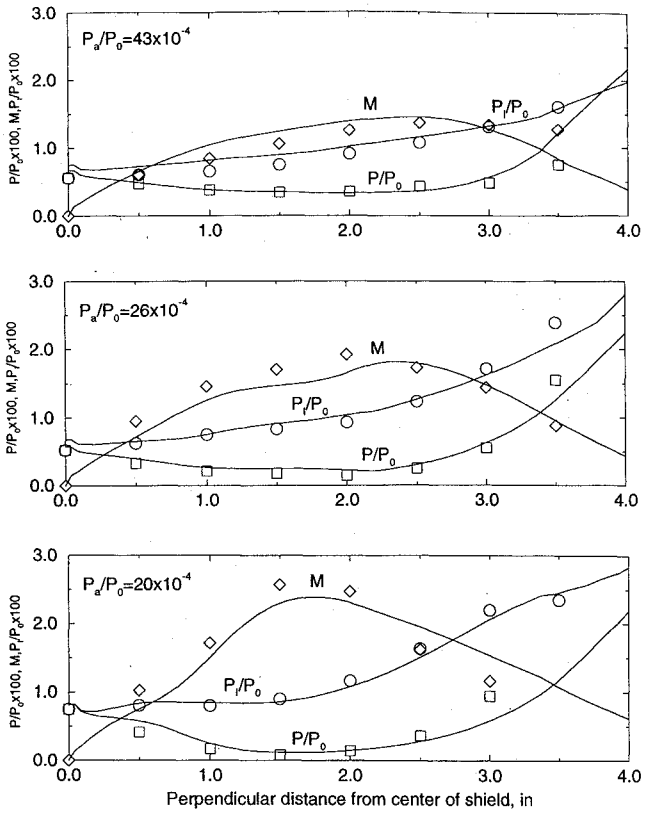

Fig. 6 Comparisons of static-pressure, Mach-number, and impact-pressure variations along model centerline: (top) □, P/P_0 test data[6]; ◊, M test data[6]; ○, P_1/P_0 test data[6]; ——, $\theta = 44.6$ deg, 119,016 pts, P adaptation; (middle) ——, $\theta = 49.0$ deg, 119,016 pts, P adaptation; and (bottom) ——, $\theta = 51.2$ deg, 168,399 pts, P adaptation.

only. However, a combination of the initial Prandtl–Meyer expansion and a solution-adaptive grid following the local flow physics leads to accurate representation of the jet in a computationally efficient manner.

Figure 6 show the comparisons of static-pressure, Mach-number, and impact-pressure variations along the model centerline for three ambient-to-total pressure ratios. In general, the predictions agreed reasonably well with those of the experiment.[6] In the supersonic flow region, where the pitot tube[6] is behind a normal shock, the Rayleigh pitot formula[35] is used to reduce the impact pressure. Although adaptive function and grid parametric studies have been performed, for the purpose of clarity only selected comparisons are shown. Different initial plume expansion angles were used to adapt the grid for different ambient-to-total pressure ratios. Notice that the initial plume expansion angle increases when the ambient-to-total pressure ratio decreases; for example, $\theta = 44.6$ deg was used for $P_a/P_0 = 43 \times 10^{-4}$, and $\theta = 51.2$ deg was used for $P_a/P_0 = 20 \times 10^{-4}$, giving results better than those obtained with one fixed angle for all pressure ratios.[10] At $P_a/P_0 = 20 \times 10^{-4}$, where the maximum model centerline base pressure and peak Mach number were measured, 168,399 grid points were required for additional resolution. The added grid points improved the prediction of the peak Mach number while not affecting base-pressure prediction. The impact pressure decreases from the plume impingement point (approximately 4.5 in. above the base, not shown) to the reverse-jet recompression location, because of nonisentropic three-dimensional flow. Downstream of the recompression, it remains constant because of the prevailing subsonic flow. In general, the peak Mach number increases and the valley static pressure decreases as the pressure ratio P_a/P_0 drops, and the position of the peak Mach number moves toward the base, as does the valley of the static pressure. The strength of the reverse jet increases as the ambient pressure drops. At $P_a/P_0 = 20 \times 10^{-4}$, a base recompression is formed between 0.5 and 1.0 in. from the base center. Because of high viscous dissipation[31] and (in general) a weak reverse jet (in comparison with an underexpanded supersonic nozzle jet impinging directly on a perpendicular surface), the base recompression tends to be a smeared shock,[6] as evidenced by the moderate rise in static pressure, albeit over a short distance, along with the observed increasingly rapid deceleration with decreasing ambient pressure.

Radial Base Pressure Distribution

Radial base pressure data were taken along the plane of symmetry between nozzles; hence the comparisons benchmark the model predictions of the reverse-jet impingement at the base center and the expansion through the vent area. It can be seen from Fig. 7 that the computed base pressures agree reasonably well with those of the experiment.[6] For all three ambient-to-total pressure ratios, the reverse jet formed and the peak pressures occurred at the base center, whereas the base pressure decreased as the distance from the center of heat shield increased. The base pressure eventually dropped to the cell pressure, which is physically correct.

Base Pressure Characteristic Curve

The center base pressure variation with ambient pressure (altitude) has become known as the characteristic curve.[6] Representing the severest environment on the base, it is one of the most important parameters in designing the thermal protection system for the launch vehicles. Figure 8 shows a comparison between the measurements and the predictions. Data[11] for an identical A_v/A_c ratio of 0.96, albeit at a mere 0.80-in. distance between the base and nozzle exit plane, were selected and plotted alongside of other data[6] for background comparison. Both experiments were conducted over the characteristic range of P_{bc}/P_a from near 1.0 to near 4.0, which corresponds to altitudes ranging from 22,800 to 122,500 ft.

At ambient-to-total pressure ratios above 100×10^{-4} or $P_{bc}/P_a < 1$, the four exhaust plumes do not interact much with each other, though some aspiration exists. As altitude increases or as pressure ratio drops, the plumes start to expand in size and the aspiration decreases. In the mean time, the base pressure decreases while a reverse jet and subsequently the wall jet take shape. The predicted base-pressure characteristic curves agreed quite well with those of the experiment.[6] The prediction of this center base pressure characteristic with wide altitude variation is a very severe test of CFD capabilities and demonstrates conclusively that all the significant flow physics has been captured. The condition

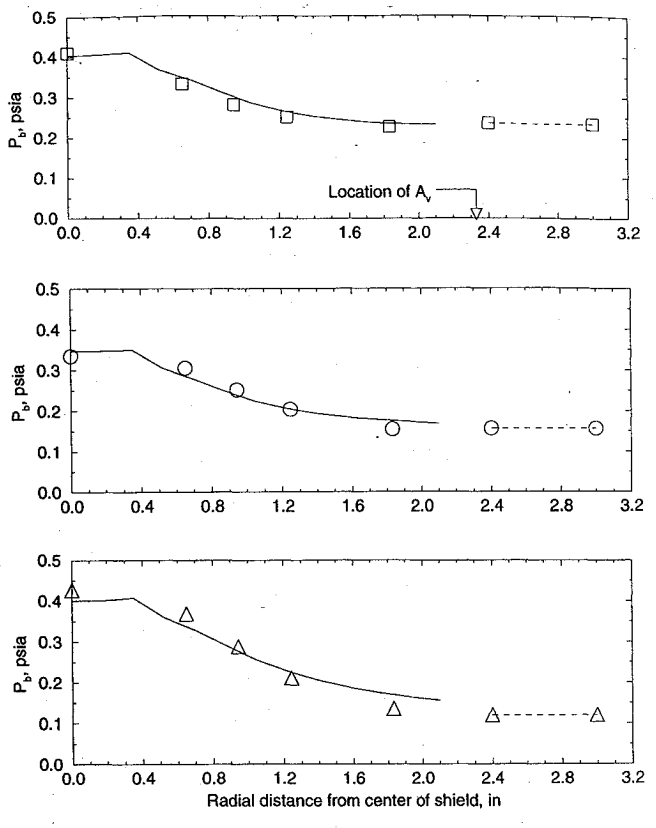

Fig. 7 Comparisons of radial base pressure distributions: (top) □, $P_a/P_0 = 39 \times 10^{-4}$ data[6]; ⊡ - ⊡, test cell pressure[6]; ——, $\theta = 45.4$ deg, 119,016 pts, P adaptation; (middle) ○, $P_a/P_0 = 26 \times 10^{-4}$ data[6]; ○ - ○, test cell pressure[6]; ——, $\theta = 49.0$ deg, 119,016 pts, P adaptation; and (bottom) △, $P_a/P_0 = 20 \times 10^{-4}$ data[6]; △ - △, test cell pressure[6]; and ——, $\theta = 51.2$ deg, 119,016 pts, M adaptation.

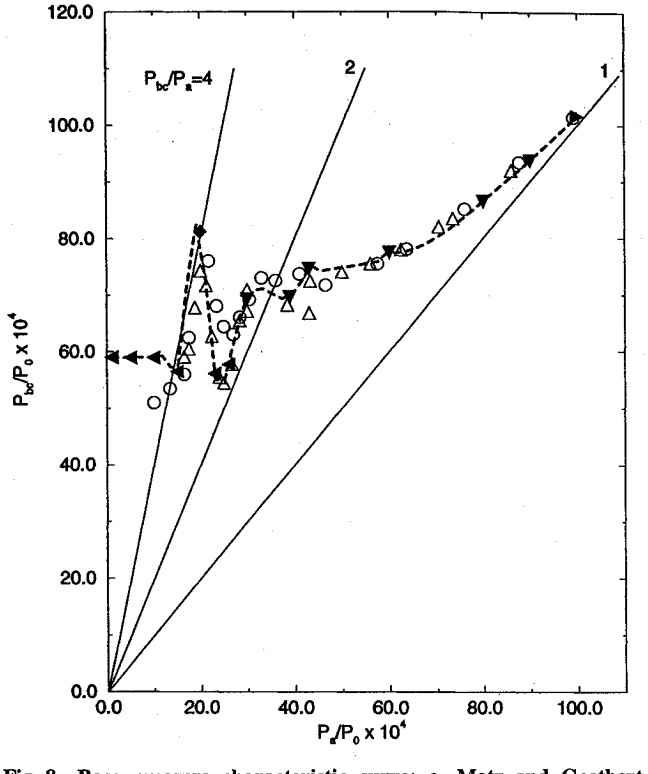

Fig. 8 Base pressure characteristic curve: ○, Matz and Goethert data[11]; △, Brewer and Craven data[6]; ◂, 119,016 pts, P adaptation; ▾, 119,016 pts, M adaptation; ▸, 119,016 pts, $0.5P + 0.5M$ adaptation; and ♦, 168,399 pts, P adaptation.

$P_{bc}/P_a = 2$ indicates choking for the wall jet if the system is an enclosed isentropic convergent–divergent nozzle; however, the choking ratio for the base flow is expected to be greater because it is three-dimensional and viscous (wall jet) and therefore a flow coefficient must be applied.

The fact that Mach-number gradient adaptation was applied for $P_a/P_0 > 26 \times 10^{-4}$, whereas pressure gradient adaptation was used at lower pressure ratios, indicates that the characteristic base pressure is better resolved by plume boundary-layer resolution when the plumes are farther apart. As the plumes close, the recompression shock becomes more important, and the center base pressure was better predicted by applying pressure gradient adaptation. The plumes close completely at $P_a/P_0 = 23 \times 10^{-4}$, where the central base pressure also reaches its minimum (Fig. 8). After that plume enclosure, the outside plume starts to enclose the vent area and leads to choking. At $P_a/P_0 = 20 \times 10^{-4}$, the reverse jet arrives at its maximum strength, and P_{bc} rises to its peak value. Afterwards, P_{bc} decreases as the ambient pressure continues to drop until the vent area is completely choked. The computed choked condition appears to occur at a nominal base-to-ambient pressure ratio of 4, corresponding to a flow coefficient of about 0.5, as evidenced by both experiments.[6,11]

Further reduction in ambient pressure did not change the base pressure, as indicated by the leveling-off of the predicted center base pressure from $P_a/P_0 = 10 \times 10^{-4}$ to 1×10^{-4}. The experiments[6,11] stopped at $P_a/P_0 = 15 \times 10^{-4}$ and 10×10^{-4}, respectively, on account of hardware limitations.

Conclusion

A computational methodology has been developed to benchmark the base flowfield of a four-engine clustered nozzle configuration. It is based on 1) a three-dimensional, viscous-flow, pressure-based CFD formulation, 2) a Prandtl–Meyer-solution treatment of the algebraic grid for the initial plume expansion resolution, and 3) a solution-adaptive grid technique that refines the computational grid subsequently according to pertinent base-flow physics. The physics of a multiple-engine clustered-nozzle base flow is significantly different from that of a single-engine base flow. These differences must be addressed to obtain accurate solutions for the clustered nozzle configuration. Qualitative features of the base flowfield of a four-engine cluster consist of a three-dimensional, turbulent reverse jet impinging upon the center of the base, forming a wall jet. This reverse jet originates from the lateral flow emanating beyond the attached shock portion of the plume-to-plume impingement line. It accelerates to supersonic speed and then smoothly decelerates to subsonic speed as it approaches the base. The deceleration becomes more rapid with decreasing ambient pressure as the peak Mach-number moves toward the base. The strength of the reverse jet is a function of the altitude and is dependent upon the Prandtl–Meyer expansion and the plume boundary-layer deflection. The flow venting between nozzles appears to choke at a nominal base-to-ambient pressure ratio of 4. Further decrease in ambient pressure does not change the base environment. The predicted physical flow features such as the reverse jet, heat-shield wall jet, recompression shock, lack of a discrete base shock, plume enclosure, and vent-area choking are in excellent agreement with those described in the experiment. The predicted quantitative results such as the radial base pressure distribution, static pressure, Mach-number and impact-pressure variations along the model centerline, and most importantly the base pressure characteristic curve, agree quite well with those of the measurement.

Acknowledgments

The author wishes to thank his colleagues Edwin Brewer for his penetrating insight into the base-flow physics and Werner Dahm for many fruitful discussions.

References

[1]Dahm, W. K., "Present Techniques and Problems in the Determination of the Base Heating Environment of Propelled Booster and Space Vehicles," *Proceedings of the 5th International Symposium on Space Technology and Science*, edited by T. Hayashi, AGNE Corp., Tokyo, 1963, pp. 377–388.

[2]Tucker, P. K., and Croteau-Gillespie, M., "Combustion Devices Technology Team: An Overview and Status of STME-Related Activities," AIAA Paper 92-3224, July 1992.

[3]Dahm, W. K., "Introduction to the Problem of Rocket Base Heating, and to the Behavior of Liquid Rocket Jet Plumes," *Molecular Radiation and Its Application to Diagnostic Techniques*, NASA TM X-53711, 1967, pp. 4–16.

[4]Bender, R. L., "Base Flow," *Rocket Exhaust Plume Technology*, edited by T. M. Gilliland, Chemical Propulsion Information Agency, Publication 263, 1981, Chap. 5, pp. 5.1.1–5.9.101.

[5]Dahm, W. K., "Relevance of Laboratory Experiments to Actual Radiating Flows," *Molecular Radiation and Its Application to Diagnostic Techniques*, NASA TM X-53711, Oct. 1967, pp. 459–473.

[6]Brewer, E. B., and Craven, C. E., "Experimental Investigation of Base Flow Field at High Altitude for a Four-Engine Clustered Nozzle Configuration," NASA TND-5164, Feb. 1969.

[7]Herrin, J. L., and Dutton, J. C., "Supersonic Base Flow Experiments in the Near-Wake of a Cylindrical Afterbody," AIAA Paper 93-2924, July 1993.

[8]Tucker, P. K., and Shyy, W., "A Numerical Analysis of Supersonic Flow over an Axisymmetric Afterbody," AIAA Paper 93-2347, June 1993.

[9]Korst, H. H., "A Theory for Base Pressures in Transonic and Supersonic Flow," *Journal of Applied Mechanics*, Vol. 23, Dec. 1956, pp. 593–600.

[10]Wang, T.-S., "Numerical Analysis of Base Flowfield for a Four-Engine Clustered Nozzle Configuration," *Journal of Propulsion and Power*, Vol. 11, No. 5, 1993, pp. 1076–1078.

[11]Matz, R., and Goethert, B. H., "Experimental Investigation of Base Flow Characteristics of Four Nozzle–Clustered Rocket Model," *Fluid Dynamic Aspects of Space Flight*, Vol. 2, edited by B. H. Goethert, Gordon and Breach, New York, 1966, pp. 223–244.

[12]Sergeant, R. J., "Base Heating Scaling Criteria for a Four-Engine Rocket Cluster Operating at High Altitude," AIAA Paper 65-826, Dec. 1965.

[13]Wilson, H. B., "A New Technique for Simulating Rocket Engine Flow for Study of Base Heating Problems," AIAA Paper 66-760, Sept. 1966.

[14]Mullen, C. R., and Bender, R. L., "Saturn V/S-IC Stage Base Thermal Environment," *Journal of Spacecraft*, Vol. 8, No. 10, 1969, pp. 1138–1143.

[15]Payne, R. G., and Jones, I. P., "Summary of Saturn I Base Thermal Environment," *Journal of Spacecraft*, Vol. 3, No. 4, 1966, pp. 489–497.

[16]Cain, T. M., Morris, N. A., Roberts, T. P., and Jones, T. V., "A Comparison of Numerical Predictions and Experiments on Under-Expanded Jets," AIAA Paper 92-4027, July 1992.

[17]Dougherty, N. S., and Liu, B., "N–S Computations with Finite-Rate Chemistry for LO2/LH2 Rocket Engine Plume Flow Studies," AIAA Paper 91-2046, Jan. 1991.

[18]Holcomb, J. E., "3-D Adaptive Grid Navier–Stokes Rocket Plume Calculations," AIAA Paper 91-0146, Jan. 1991.

[19]Sindir, M., and Lynch, D., "NLS Base Heating CFD Analysis," Rockwell International, IL 92RC07980; National Launch System Base Heating Technical Interchange Meeting, Marshall Space Flight Center, AL, July 1992.

[20]Shyy, W., and Sindir, M., "Comments on Policy Statement on the Control of Numerical Accuracy," *Journal of Fluids Engineering*, Vol. 115, June 1994, pp. 196–197.

[21]Launder, B. E., and Spalding, D. B., "The Numerical Computation of Turbulent Flows," *Computer Methods in Applied Mechanics and Engineering*, Vol. 3, No. 2, 1974, pp. 269–289.

[22]Monson, D. J., Seegmiller, H. L., McConnaughey, P. K., and Chen, Y.-S., "Comparison of Experiment with Calculations Using Curvature-Corrected Zero and Two Equation Turbulence Models for a Two-Dimensional U-Duct," AIAA Paper 90-1484, June 1990.

[23]Chen, Y.-S., Cheng, G. C., and Farmer, R. C., "Reacting and Non-Reacting Flow Simulation for Film Cooling in 2-D Supersonic Flows," AIAA Paper 92-3602, July 1992.

[24]Wang, T.-S., "Numerical Study of the Transient Nozzle Flow Separation of Liquid Rocket Engines," *Computational Fluid Dynamics Journal*, Vol. 1, No. 3, 1992, pp. 305–314.

[25]Wang, T.-S., and Chen, Y.-S., "Unified Navier–Stokes Flowfield and Performance Analysis of Liquid Rocket Engines," *Journal of Propulsion and Power*, Vol. 9, No. 5, 1993, pp. 678–685.

[26]Wang, T.-S., and Luong, V., "Hot-Gas-Side and Coolant-Side Heat Transfer in Liquid Rocket Engine Combustors," *Journal of Thermophysics and Heat Transfer*, Vol. 8, No. 3, 1994, pp. 524–530.

[27]Liakopouls, A., "Explicit Representations of the Complete Velocity Profile in a Turbulent Boundary Layer," *AIAA Journal*, Vol. 22, No. 6, 1984, pp. 844–846.

[28]Wang, T.-S., and Chyu, M.-K., "Heat Convection in a 180-deg Turning Duct with Different Turn Configurations," *Journal of Thermophysics and Heat Transfer*, Vol. 8, No. 3, 1994, pp. 595–601.

[29]Jorgenson, P., and Turkel, E., "Central Difference TVD Schemes for Time Dependent and Steady State Problems," *Journal of Computational Physics*, Vol. 107, No. 2, 1993, pp. 297–308.

[30]Liou, M. S., and Steffen, C. J., "A New Flux Splitting Scheme," *Journal of Computational Physics*, Vol. 107, No. 1, 1993, pp. 23–39.

[31]Wasco, R. A., and Cover, T. L., "Experimental Investigation of Base Flowfield at High Altitudes for Configurations of Four and Five Clustered Nozzles," NASA TM X-1371, 1967.

[32]Soni, B. K., Thompson, J. F., Stokes, M. L., and Shih, M.-H., "GENIE++, EAGLEView and TIGER: General and Special Purpose Interactive Grid Systems," AIAA Paper 92-0071, Jan. 1992.

[33]Chen, Y.-S., Liaw, P., Shang, H.-M., and Chen, C.-P., "Numerical Analysis of Complex Internal and External Viscous Flows with a Second-Order Pressure-Based Method," AIAA Paper 93-2966, July 1993.

[34]Childs, R. E., and Caruso, S. C., "On the Accuracy of Turbulence Base Flow Predictions," AIAA Paper 87-1439, June 1987.

[35]Ames research staff, "Equations, Tables, and Charts for Compressible Flow," NACA Rept. 1135, 1935.

[36]Svehla, R. A., and McBride, B. J., "FORTRAN IV Computer Program for Calculation of Thermodynamic and Transport Properties of Complex Chemical Systems," NASA TN D-7056, 1973.

[37]Davies, C. B., and Venkatapathy, E., "The Multidimensional Self-Adaptive Grid Code: SAGE," NASA TM 103905, July 1992.

T. C. Lin
Associate Editor